Resonant Raman-Compton scattering on zirconium

A. Simionovici,* J. P. Briand, P. Indelicato,† and P. Chevallier
Laboratoire de Physique Atomique et Nucléaire–Institut du Radium, Université Pierre et Marie Curie, 4 place Jussieu, 75252 Paris CEDEX 05, France
(Received 12 April 1989; revised manuscript received 20 November 1989)

Resonant Raman-Compton scattering has been studied with synchrotron radiation in the vicinity of the K absorption edge of zirconium. The full spectrum, including the infrared divergence has been studied in a wide energy range on targets of various thicknesses. Absolute cross sections have been measured and compared to theoretical calculations.

I. INTRODUCTION

Mainly due to historical reasons (experimental setup, energy range, and momentum-transfer regime) the various manifestations of inelastic scattering of photons by electrons have received different names and an incomplete definition of the final state has often led to some confusion. In the x-ray energy range, the inelastic scattering of photons is usually dominated by the Compton effect on free or quasifree atomic electrons. When considering electrons in quantized bound states, the inelastic scattering of photons may proceed through Raman effect, where the energy lost by the incoming photon is used to excite the atomic target into a bound state. This (nonresonant) Raman scattering, well known in molecular physics, was first observed in the x-ray regime in 1959 by Das Gupta.[1] In the x-ray energy domain where the inner-core electrons can be excited to autoionizing states, the energy lost by the impinging photon is used to simultaneously ionize and excite the atom. In this case, the available energy, i.e., the incident energy minus the excitation energy of the atom in its final state, is shared, in a continuous way, between the scattered photon and the ejected electron. When the energy of the incoming photon is close to that of a discrete, real, excited state of the atom, the process has a resonant character. This resonant behavior was first demonstrated in 1974 by Sparks, Jr.[2] by studying various metallic targets of different ionization energies irradiated by a fixed-energy source. When the excited state is close to the continuum, both the resonant Raman scattering (scattering of a monoenergetic photon) and the resonant Raman-Compton scattering, in which the available energy is shared between an ejected electron and the scattered photon (continuum spectra) may be expected. When the inner-shell electrons ($L,M,\ldots$) of metallic targets are excited near the continuum, where the discrete states merge into energy bands, the resonant Raman scattering cannot be separated from the Raman-Compton scattering. However, these two effects were separately observed for the first time in 1981 by Briand *et al.*[3] and their different resonant behaviors have been studied using a compound target ($KMnO_4$). In this instance the site of the resonance was the $3t^2$ discrete quasimolecular level of the MnO_4 ion, which has a predominant $4p$ atomic manganese character.

We present in the paper some experiments carried out with the synchrotron radiation delivered by the Laboratoire pour l'Utilisation du Rayonnement Electromagnétique DCI storage ring (LURE DCI) facility in Orsay, France where the resonant Raman-Compton scattering (RRCS) has been studied in the vicinity of the K absorption edge of zirconium. In these experiments, we have studied the shape of the emitted continua, including the infrared divergence (ID) recently observed by Briand *et al.*[4] as a function of the incoming photon energy and the absolute cross sections of RRCS that we have compared to theoretical predictions.

II. THEORY

A. Formalism

In order to describe the scattering process we define the usual quantum-mechanical picture: the atom coupled to the photon field derived from Maxwell's equations in the Coulomb gauge. We shall describe this system by the total Hamiltonian H:

$$H=\sum_{j=1}^{Z}\frac{1}{2m}\left[\mathbf{P}_j-\frac{e}{c}\mathbf{A}(\mathbf{r}_j)\right]^2+V(\mathbf{r}_j)+H_\nu\ . \tag{1}$$

Here m stands for the electron mass at rest, $\mathbf{A}$ is the vector potential of the field, $\mathbf{P}$ the electronic momentum operator, V the atomic potential, H_ν the Hamiltonian of the free photon field, and the sum is taken over the Z atomic electrons. We can subsequently isolate the part of the Hamiltonian which describes the interaction between the atom and the photon field:

$$H_i=\sum_{j=1}^{Z}\left[\frac{-e}{mc}\mathbf{P}_j\cdot\mathbf{A}(\mathbf{r}_j)+\frac{e^2}{2mc^2}\mathbf{A}^2(\mathbf{r}_j)\right]\ . \tag{2}$$

Following, for example, Sakurai,[5] by applying Fermi's golden rule we obtain the modified Kramers-Heisenberg-Waller (KHW) formulas for the scattering cross section:

$$\left[\frac{d^2\sigma}{d\nu_2 d\Omega_2}\right]_{I\to F}=2\pi r_0^2\frac{\nu_2}{\nu_1}\left|\langle F|e^{i\mathbf{k}\cdot\mathbf{r}}|I\rangle(\mathbf{e}_1\cdot\mathbf{e}_2^*)-\frac{1}{m}\sum_N\left[\frac{\langle F|\mathbf{P}\cdot\mathbf{e}_2^*|N\rangle\langle N|\mathbf{P}\cdot\mathbf{e}_1|I\rangle}{E_N-E_I-h\nu_1-\frac{i}{2}\Gamma_N}+\frac{\langle F|\mathbf{P}\cdot\mathbf{e}_1|N\rangle\langle N|\mathbf{P}\cdot\mathbf{e}_2^*|I\rangle}{E_N-E_1+h\nu_2-\frac{i}{2}\Gamma_N+\frac{i}{2}\Gamma_1}\right]\right|^2 \tag{3}$$

where $|I\rangle$, $|F\rangle$, and $|N\rangle$ represent, respectively, the initial, final, and intermediate states (real or virtual), ν_1 and ν_2 stand for the frequencies of the incident and scattered photons, Ω_2 the solid angle, r_0 the classical electron radius, $\mathbf{k}$ the photon momentum transfer, $\mathbf{e}_1$ and $\mathbf{e}_2$ the photon polarizations. The initial and intermediate levels are depleted in the time $\tau_{I,N}=(\hbar/\Gamma_{I,N})^{-1}$ and by Γ we have denoted the natural widths of the states. The dipolar approximations ($e^{ikr}=1$) has been used to obtain the last two terms of this formula which is justified when the wavelengths of the incident and scattered photons are large compared to the size of the corresponding atomic shell.

B. Resonances

The first term of formula (3) is taken at the first order of the perturbation theory and is known as the A^2 term in literature. This term is dominant when the incident energy ($h\nu_1$) is far greater than the electronic binding energies and describes the nonresonant scattering processes as the "free" electron Compton effect, the Raman effect, or the elastic scattering. The contribution of the A^2 term to the total cross section may be important in the off-resonance region ($0<h\nu_1<B_K$) as it has been shown by Åberg and Tulkki[6] in the case of $2p$ electrons, especially at $\theta=90°$, experimental geometry chosen for most of the experiments to date. It is thus important to include it in any complete calculation of the scattering at intermediate energies, or, as we will further show, to minimize it if only resonance effects are of interest.

When the incident energy is comparable to the electronic binding energies, resonance phenomena may occur due to the last two terms of Eq. (3) known as the $\mathbf{P}\cdot\mathbf{A}$ terms. These terms are taken at the second order of perturbation theory, their contribution to the first order being zero. To explain resonances which occur when the incident energy approaches the K-shell binding energy, a simple mechanism was proposed[7,8] using intermediate states, corresponding to the excitation of a K-shell electron into an unoccupied level and a final state with an L-shell hole. If an electron is, in the final state, in the continuum the process is called the Raman-Compton effect (L-shell Compton effect); if this electron is on a discrete excited level the corresponding process is the resonant Raman effect.

A schematic representation of these processes appears in Fig. 1 where for the sake of clarity we consider only one $2p$ atomic level. When considering the resonant Raman effect, a K electron is excited to a virtual state N located at an energy ε_1 from a discrete atomic level ($1s^{-1}np^{+1}$ state). A monoenergetic photon is scattered and the atom is left in a $2p^{-1}np^{+1}$ excited states. The energy of the Raman line is $(h\nu_2)_R=h\nu_1-E(2p^{-1}np^{+1})$, which is almost equal to $E_{K\alpha}-\varepsilon_1$.

In the Raman-Compton effect [Fig. 1(b)], erroneously labeled "resonant Raman effect" in the literature, the K electron is excited into the virtual state (N) located at an energy ε_2 from the K ionization threshold. In the course of the deexcitation, an electron and a (scattered) photon, (L to K transition) are emitted thus leaving the atom in an excited state with an L-shell hole. The photon will thus have the energy of the characteristic $K\alpha$ transitions minus ε_2 and the electron kinetic energy E_c (Fig. 1). The sharing of the available energy between the two emitted particles gives rise to an asymmetric continuum in the spectra of either the electron or the photon.

For incident energies $h\nu_1=E_N-E_I$, the second term of Eq. (3) has a maximum as its denominator tends to zero, the classical divergence being avoided thanks to the natural width of the intermediate level. If E_N corresponds to a *real* excitation level of the atom, one observes the fluorescence resonance.[9] This quite sharp resonance occurs in a reduced energy range around the considered discrete level. The first experiment in which this resonance has been observed and identified as a *pure* resonant Raman effect together with the Raman-Compton resonance was the one by Briand *et al.*[3] In fact this effect can only be observed in high-resolution measurements, as it spreads only a few eV around the intermediate state and because the Raman line lies very near the fluorescence line. Since then evidence for this effect has also been given by Deslattes[10] near the K threshold of Ar and S.

In the case of the Raman-Compton scattering the photon energy spectrum is continuous and has a sharp high-energy cutoff. This maximum occurs at an energy of $K\alpha-\varepsilon_2$ ($h\nu_1-B_L$ where B_L is the L electron binding energy) or when the electron is emitted in the continuum with zero kinetic energy. This maximum, easily observable in the spectrum of the scattered photons, is the sig-

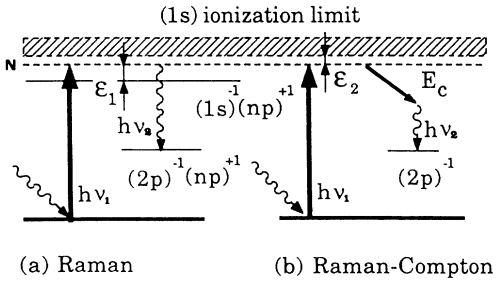

FIG. 1. Resonant Raman-Compton scattering (a) Raman scattering (inelastic scattering of a photon); (b) Raman-Compton scattering (the energy given to the atom is, in the final state, shared between an electron and a photon).

nature of the Raman-Compton effect. Its asymmetrical shape is characterized by a decrease with the energy of the scattered photon as $(B_K - B_L - h\nu_2)^{-2}$.[8] At resonance, when the incident energy is equal to that of the K electron ionization ($\varepsilon_2 = 0$), this process evolves into the K-shell fluorescence. As shown by Tulkki and Åberg[9] this change is continuous over a range of energies in the vicinity of the K threshold where the cross sections of the two processes become equal. The other specific contribution to the Raman-Compton effect occurs, at the other end of the scattered photon spectrum, when the electron emitted in the continuum takes almost all the available energy and the photon of energy $h\nu_2 \to 0$ gives rise to the infrared divergence.[4] The cross section dramatically increases for vanishing energies of the scattered photon, a phenomenon known as the infrared catastrophe in classical electrodynamics.

Following Gavrila and Tugulea[11] if a $2p$ electron is ejected in the continuum a resonance due to the third term of Eq. (3) will occur for incident energies greater than or equal to the K-shell binding energy. We have not investigated this effect in the present experiment because it needed monochromatic photons of energy higher than what could be reached with our monochromator.

C. Calculations

There are substantial difficulties in calculating the cross section from Eq. (3). The wave functions of the excited and intermediate bound states, the final continuum states, all represent so many obstacles in the way of an exact calculation. In 1975, Gavrila and Tugulea[11] calculated the Raman-Compton effect cross section for the scattering on L electrons using the Kramers-Heisenberg-Waller formulas as a starting point. The KHW matrix elements are calculated nonrelativistically, in a purely Coulomb atomic field. A hydrogenlike model is used for the atom and Green's function is taken for the Coulomb field. Both the intermediate and the continuum wave functions are described by Schwinger's integral representation. Moreover, the calculations can be made almost entirely in an analytical manner if the dipolar approximation is used. In this case, the nonresonant term of Eq. (3) is null due to the orthogonality of the initial- and final-state wave functions. The remaining terms are thus considerably simplified and the KHW formulas can be reduced to the case of a hydrogenic atom. The calculations are carried out separately for the $2s$ and $2p$ electrons and simple expressions for the double differential cross sections (in both scattered photon energy and solid angle) are derived. Their results are

$$\frac{d^2\sigma_{2s}}{d\chi_2 d\Omega_2} = \frac{r_0^2}{2}(C_1' + C_2'\cos^2\theta) ,$$
$$\frac{d^2\sigma_{2p}}{d\chi_2 d\Omega_2} = \frac{r_0^2}{2}(C_1'' + C_2''\cos^2\theta) , \tag{4}$$

where θ is the angle between the incident and scattered photon and $\chi_{1,2}$ are the incident and scattered photon energies in threshold units ($\chi_{1,(2)} = E_{1,(2)}/B_K$). The C coefficients are functions of χ_1 and χ_2 and are tabulated for a large range of energies. These formulas are established in the case of unpolarized photons and undetected ejected electrons, the corresponding relation being

$$\frac{d^2\sigma}{dE_2 d\Omega_2} = \tfrac{1}{2}\sum_{e_1,e_2}\int_{\Omega_2}\frac{d^3\sigma}{dE_2 d\Omega_2 d\Omega_e}d\Omega_e , \tag{5}$$

where the average is taken over the initial polarizations, the sum over the final polarizations, and the integral over the solid angle of the ejected electron Ω_e. A numerical calculation based upon this formulation was carried out in 1975 and the results were tabulated in an easily usable form.[11] We present in Figs. 2(a) and 2(b) the variation of the C coefficients as a function of the scattered photon energy. The cross sections for both $2s$ and $2p$ electrons exhibit an obvious infrared divergence when the energy of the scattered photon vanishes and the $2p$ cross section

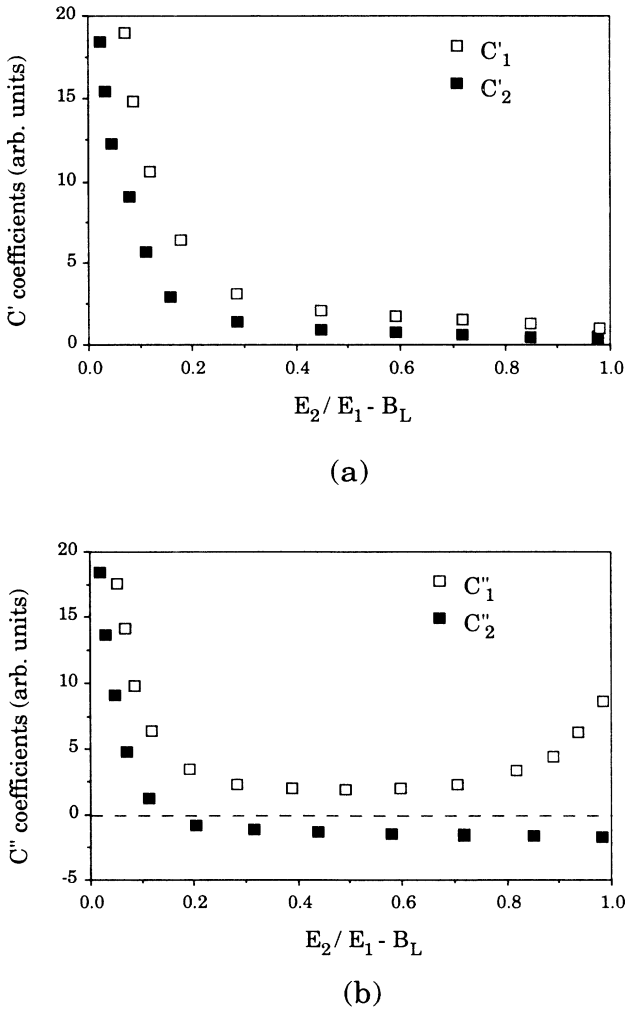

FIG. 2. (a) C' coefficients for the $2s$ electrons as a function of the scattered photon energy E_2 (from formula 4). (b) C'' coefficients for the $2p$ electrons as a function of the scattered photon energy E_2 (from formula 4).

(the dominant one) has also an almost isotropical character, given $C_1''/C_2'' \gg 1$.

D. Application to our experimental case

Our specific experimental conditions imposed a number of modifications to the rather general theoretical formulations of Gavrila and co-workers. We will present the corrections to the above treatment that we derived for the experimental situation encountered in synchrotron radiation studies.

Unlike Bannett *et al.*[12] who used an unpolarized x-ray source (Cu $K\alpha$ radiation), we had an almost totally polarized ($>99.9\%$) source of radiation provided by synchrotron light, and monochromatized by a Si(220) channel cut. The corresponding geometry, exhibiting the photon directions of propagation and their polarizations, is presented in Fig. 3. The first term of Eq. (3), which contains the scalar product of the initial and final polarizations ($\mathbf{e}_1 \cdot \mathbf{e}_2$) vanishes due to the orthogonality of the polarizations of the incoming and scattered photons (Fig. 3). We are then in the situation described by the theoretical calculation, where the nonresonant contribution to the scattering is negligible and a direct comparison is allowed.

The hydrogenic model used imposed energy restrictions ($B_K = 4B_L$) that were incompatible with the multielectron experimental case. We were thus forced to use multielectron binding energies in the derivation of the cross sections.

The drawback of using polarized incident radiation was that the cross sections had to be recalculated in this particular case. In a more general way we had to evaluate

$$\frac{d^2\sigma}{dE_2 d\Omega_2} = \sum_{e_2} \int_{\Omega_e} \frac{d^3\sigma}{dE_2 d\Omega_2 d\Omega_e} d\Omega_e \ , \tag{6}$$

a formula slightly different from the one derived in Gavrila's papers as we do not average over the initial polarizations any more. The triple differential cross sections are given by

$$\begin{aligned} \frac{d^3\sigma_{2s}}{dE_2 d\Omega_2 d\Omega_e} &= \frac{r_0^2}{B_K}\frac{E_2}{E_1}|M_{2s}|^2 \ , \\ \frac{d^3\sigma_{2p}}{dE_2 d\Omega_2 d\Omega_e} &= \frac{1}{3}\frac{r_0^2}{B_K}\frac{E_2}{E_1}\sum_{\alpha}|M_{2p}^{\alpha}|^2 \ , \end{aligned} \tag{7}$$

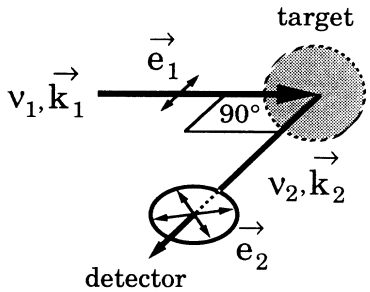

FIG. 3. Schematic of the polarizations and wave vectors for the RRC scattering (see text).

where the matrix elements for the scattering over $2s$ and $2p$ electrons appear and $\alpha = x,y,z$. We can then establish new expressions for the C coefficient in the case of an incident beam totally polarized in the scattering plane ($\mathbf{K}_1$, $\mathbf{K}_2$ plane) and a nonpolarized scattered photon at an angle θ. Their expressions are as follows:

$$\frac{d^2\sigma_{2s,2p}}{dE_2 d\Omega_2} = \frac{r_0^2}{2B_K}[C_1^{\mathrm{pol}}(2s,2p) + C_2^{\mathrm{pol}}(2s,2p)\cos^2\theta] \ . \tag{8}$$

Fortunately, the final result can be factorized in terms of the C coefficients tabulated in Ref. 11 (see Ref. 13). Furthermore, if we make use of the fact that for our experiment $\theta = 90°$ (which implies that $\mathbf{e}_1 \perp \mathbf{e}_2$) the angular contributions in the formula vanish, and using the same notations from Ref. 11, the polarized incident photon cross sections are simply

$$C_1^{\mathrm{pol}}(2s) = C_1' - C_2' \quad \text{and} \quad C_2^{\mathrm{pol}}(2s) = 2C_2' \ , \tag{9}$$

$$C_1^{\mathrm{pol}}(2p) = C_1'' - C_2'' \quad \text{and} \quad C_2^{\mathrm{pol}}(2p) = 2C_2'' \ , \tag{10}$$

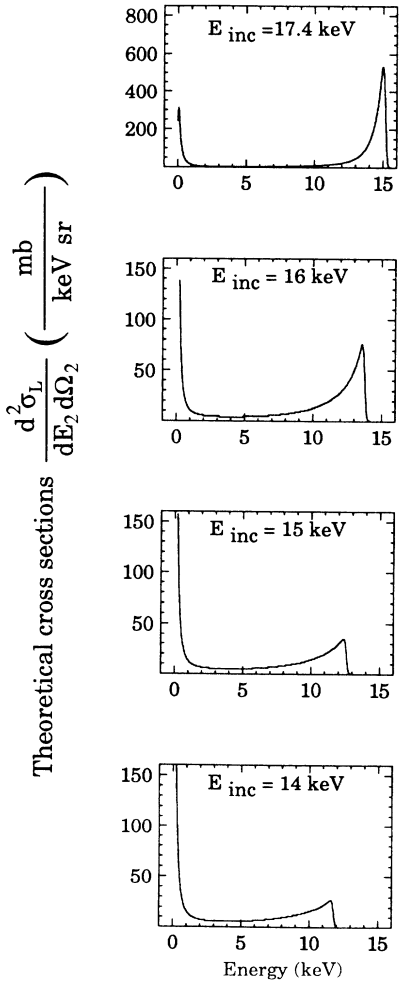

FIG. 4. Theoretical RRC differential cross sections for several incident photon energies as a function of the scattered photon energy.

$$\frac{d^2\sigma_{2s}}{dE_2 d\Omega_2}=\frac{r_0^2}{2B_K}(C_1'-C_2'),$$
$$\frac{d^2\sigma_{2p}}{dE_2 d\Omega_2}=\frac{r_0^2}{2B_K}(C_1''-C_2'')\ . \tag{11}$$

Finally, we can write the total scattering cross section on L-shell electrons as

$$\frac{d^2\sigma_L}{dE_2 d\Omega_2}=2\frac{d^2\sigma_{2s}}{dE_2 d\Omega_2}+6\frac{d^2\sigma_{2p}}{dE_2 d\Omega_2}$$
$$=\frac{r_0^2}{B_K}[(C_1'-C_2')+3(C_1''-C_2'')]\ . \tag{12}$$

For a direct comparison with the experimental cross sections we have convoluted the calculated spectra with an instrumental transmission function, which for our spectrometer is approximately a Gaussian function with a full width at half maximum which increases like $\sqrt{E}$ (detected photon energy). We present in Fig. 4 the calculated double differential cross sections (in units of mb/keV/sr), for our experimental conditions.

III. EXPERIMENTS

A. Description

The purpose of the experiment which is presented in Fig. 5 is to irradiate very thin zirconium targets by the photons delivered by the LURE DCI synchrotron radiation facility and to observe the scattered spectra at 90°. with respect to the photon beam. The continuous x-ray spectrum delivered by the DCI storage ring operating at an energy of 1.8 GeV with 200 mA of positron beams was monochromatized by a Si(220) channel-cut crystal. This photon beam whose bandpass was of the order of a few eV and intensity of the order of 10^9 photons/sec, was sent on very thin (20–200 μg/cm^2) zirconium targets on 1.5-μm Mylar backings. The scattered spectra were analyzed in a high-resolution [full-width at half maximum (FWHM) of 165 eV at 5.9 keV] SiLi detector located in the electron orbital plane and at 90° from the incident beam. The experimental ensemble was carefully aligned allowing a precision in the beam position measurement of ± 100 μm or ± 1 min on the angles. The whole experimental setup was moved up and down to fit with the beam elevation when the energy was changed. In order to be able to study the whole continuous scattered spectrum from the lowest energies (the infrared region) up to the high-energy profile, the assembly was mounted under vacuum and a detector with a very thin (25 μm) beryllium window was used. The choice of the atomic number of the target which must be the highest possible, was defined by the highest available energy delivered by the channel cut (19 keV), leading us to use zirconium ($Z=40$) whose K-shell ionization energy is approximately 18 keV. We have studied the RRCS around the K resonance energy for $2p^{-1}nl^{+1}$ final excited states. In such a case the full scattered spectra extended from $h\nu_1-B_L$ ($B_L\approx 2.5$ keV) down to ≈ 1.4 keV (low-energy threshold of the detector).

The efficiency of the SiLi detector (including the Be window, gold contact, and the Si lead layer) was experimentally measured in the energy range of 1.5–9 keV. The method we used was to take advantage of the synchrotron light itself to provide standard x-ray fluorescence sources. We used the photon beam delivered by the channel-cut monochromator to excite the fluorescence of various, very thick targets (Al, S, Ti, Cr, Fe, Ni, Zn, Ge). Owing to the very high stability of the photon beam of DCI (which was monitored separately) it was possible to accurately measure the total efficiency of the detector as shown in Fig. 6.

B. Data reduction

We present in Fig. 7 a typical spectrum recorded for 17.4 keV incoming photon energy, where all the photon interaction processes can be seen. The main line observed (L x-ray spectrum) originates from the L photoionization of Zr which is the most important process at energies below the K ionization limit. One can also see

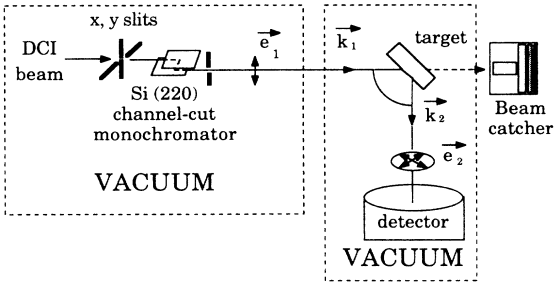

FIG. 5. Schematic of the experimental setup.

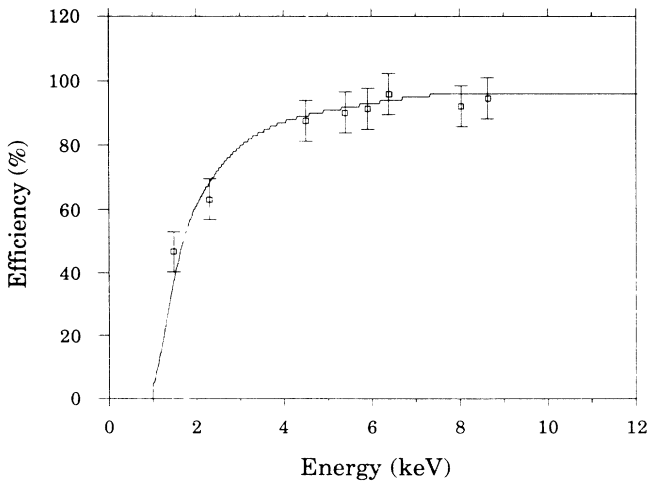

FIG. 6. Measured detector efficiency as a function of the photon energy. Squares denote experimental points; the smooth curve is a constrained fit to the data.

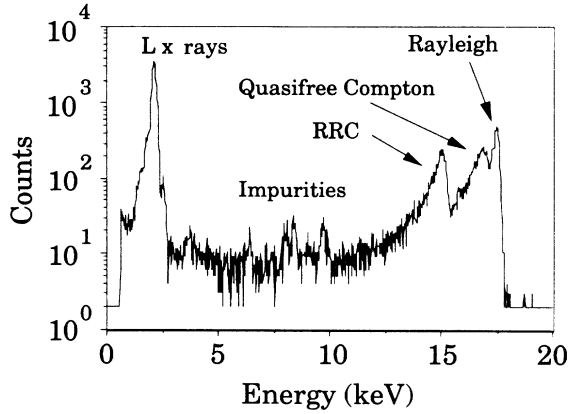

FIG. 7. Typical raw spectrum at incident energy $E=17.4$ keV.

on this spectrum the Rayleigh peak (elastic scattering) at the energy of the incoming photon, the free (or quasifree) electron Compton profile, and the high-energy profile of the RRCS at an energy of $17.4-B_L \approx 15$ keV. In addition to these lines and continua, some fluorescence lines corresponding to impurities (<100 ppm) contained in the Zr target can be observed in the intermediate-energy region (the low-energy rise which can easily be observed will be discussed below). These scattering processes have been minimized in intensity by observing the spectra in the polarization plane and at 90° from the incident beam, a scattering angle for which both the Rayleigh and the Compton peaks are at their lowest.

The absolute intensities of the continua to be studied have been determined in the following way: at each incoming energy from 14 to 18 keV we recorded the fluorescence spectrum of a very pure Fe thick target, in the same geometry as for the RRCS samples. It was then possible, using the previously measured detector efficiency and the photoionization cross sections available in the literature[14] to calibrate the photon beam and thus correct for the steady drop in intensity over the time, due to the limited lifetime of the positron beam in the synchrotron (over 40 h). The result of these measurements is an absolute parameter: $N_0\Delta\Omega$ equal to the product of the number of incident photons arriving on the target by the solid angle viewed by the detector. The RRCS cross sections are then directly compared to photoionization cross sections which then provide the best theoretical checks. The precision of this absolute intensity calibration for the scattering cross section is a function of the incoming energy. At low energies, due to the uncertainties in the total absorption cross sections as well as the detector efficiency and target thicknesses, the precision varies between 15 and 20% while on the high-energy end of the RRCS the total uncertainties vary between 8% and 15%.

One of the most difficult parts of the experiment is the study of the low-energy rise to the RRCS continuum which might also be caused by other spurious processes. As described in Ref. 4, the most intense predictable cause for such a rise at low energy is the bremsstrahlung emitted during the slowing down of the L photoelectrons produced in the target as the L photoionization is (by orders of magnitude) the most important process during the photon interactions. This process has been extensively studied in Ref. 4 and found to be negligible. The way in which we studied this low-energy background is the following: we first used very thin Zr targets (20 μg/cm^2) such that the range of the L photoelectrons is much larger than the target thickness in order to minimize the bremsstrahlung process. We present in Table I the range of the L photoelectrons in zirconium targets as a function of the incoming x-ray photons, derived from semiempirical calculations.[15,16] The observed spectra were then compared to those obtained with much thicker ones (200 μg/cm^2) in which the ejected photoelectrons could be strongly slowed down. It was then possible to accurately establish that the low-energy rise did not originate from the L photoelectron bremsstrahlung but mainly from the RRCS itself. Owing to the very long exposure times when using very thin targets (15–20 h, i.e., of the order of magnitude of the lifetime of the positron beam in the storage ring) we mainly used the thicker targets to study the RRCS on a large range of energies. In order to get rid of all the spurious processes appearing in the spectra (Rayleigh and Compton scattering, fluorescences of the impurities, and L x-rays), all the characteristic spectra of these processes were separately studied (with a variety of targets irradiated in the same experimental conditions), in order to be subtracted from the experimental data (including their low-energy tails). The L x rays and the spurious fluorescences were fitted with Gaussian shapes plus quadratic backgrounds and thus subtracted from the raw spectra. The residuals were then normalized at the statistic ($\sqrt{N}$) noise of the surrounding background. Once these corrections were performed on the spectra (which were already corrected for the detector efficiency) we established the following formulas for deriving the experimental RRCS cross section:

$$d^3N(x,E,\Omega)=N_0 e^{-\mu(E_0)(x/\sin\alpha)}\frac{d^2\sigma_c}{dE d\Omega}n \times\frac{dx}{\sin\alpha}dE\,d\Omega e^{-\mu(E)(x/\sin\alpha)} \quad (13)$$

where d^3N is the number of photons arriving on the detector in the solid angle comprised between Ω and $\Omega+\Delta\Omega$ (Fig. 8), emitted by the layer of thickness dx inside the target, and having an energy between E, and

TABLE I. Range of L photoelectrons in zirconium as a function of the incident photon energy (from Ref. 15).

x-ray energy (keV)	L electron range (μg/cm^2)
17.4	529
16.4	475
15.4	423
14.4	378
13.4	332

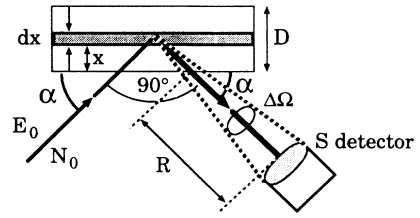

FIG. 8. Schematic of the scattering geometry.

$E+dE$. N_0 is the number of incident photons of energy E_0 and the total absorption coefficients for the different energies are noted by μ. Also the RRCS cross section is noted by σ_c and n is the atomic density of the target. The two exponentials characterize, respectively, the absorption of the incident and scattered photons in the target. Integrating the previous formula over x between zero and D the target thickness and over Ω in the solid angle $\Delta\Omega$ subtended by the detector, one obtains

$$dN(E)=N_0 n\frac{1-e^{[(\mu_0+\mu_E)/\sin\alpha]D}}{\mu_0+\mu_E}\left|\frac{\overline{d^2\sigma c}}{dE\,d\Omega}\right|_{\alpha=90^\circ}\Delta\Omega\,dE\ . \tag{14}$$

Here the differential cross section is averaged, and its value is taken at $\theta=90°$. Then the experimental spectrum S (channels) is straightforwardly obtained if the calibration slope is denoted by dE/dc (keV per channel):

$$\frac{dN(E)}{dE}=\frac{S(c)}{dE/dc}\ . \tag{15}$$

The final expression of the RRCS experimental cross section then becomes

$$\left|\frac{\overline{d^2\sigma_c}}{de\,d\Omega}\right|_{\alpha=90^\circ}=\frac{S(c)}{(dE/dc)N_0\Delta\Omega n}\frac{\mu_0+\mu_E}{1-e^{-[(\mu_0+\mu_E)/\sin\alpha]D}}\ . \tag{16}$$

The normalization parameter $N_0\Delta\Omega$ which has been discussed previously provides the absolute intensity scale for the cross section (b/keV sr). These procedures were independently checked on several test cases and found to yield consistent results on the energy range scanned by the experiments.

C. Experimental results

Our experimental results were obtained for the following incident energies: 17.4, 16, 15, and 14 keV. The target used were zirconium 200 $\mu g/cm^2$ foils obtained by vacuum deposition on 1.5-μm Mylar films. In two separate cases ($E_i=15$ and 16 keV), independent measurements were performed on very thin targets (20 $\mu g/cm^2$) which provided consistency checks for the thicker foils. The results are presented in Fig. 9 for the four different energies using the thicker targets. The absolute differential cross sections as a function of the scattered photon energy and solid angle are scaled in units of b/keV sr. The vertical scale is the same as that of the theoretical spectra for easy comparison.

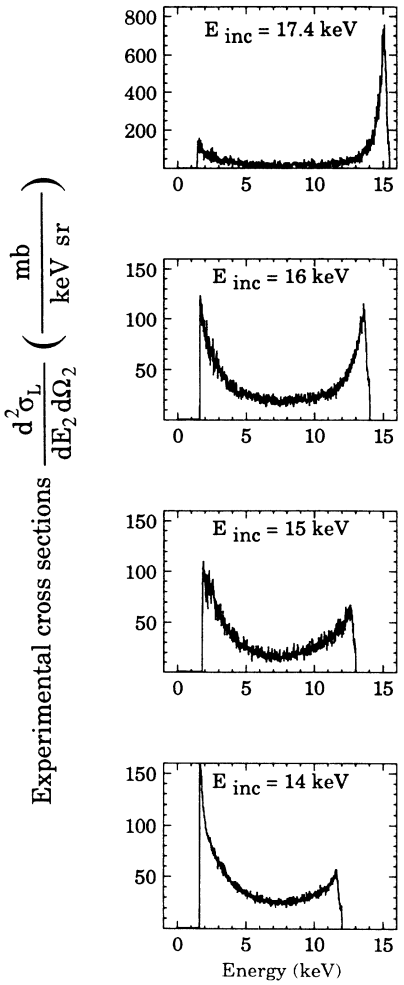

FIG. 9. Experimental RRC differential cross sections for several incident photon energies as a function of the scattered photon energy.

IV. DISCUSSION

To date, there are only few experiments similar to the ones presented here. This is mainly due to the experimental difficulties encountered and to the absence of comprehensive theoretical predictions for this energy region. Our results are thus original in several aspects: minimization of spurious effects (bremsstrahlung, fluorescences, Rayleigh, and quasifree Compton scattering, etc.) due to the reduced target thicknesses, accurate absolute efficiency calibration, use of polarization effects to optimize the signal to noise ratio (reduction of the Rayleigh and Compton scattering when observed at 90°) and to eliminate the nonresonant contribution to the scattering, and calculations of the differential cross sections including the polarization effects.

When comparing the experimental results (Fig. 9) with theory (Fig. 4), one must separately analyze the shape of

the RRC (high photon energy) and of ID (low photon energy). Generally speaking, we observe on all our spectra a qualitative agreement with the theoretical predictions (changes in shape as a function of the incoming energy). Quantitatively though, the agreement seems to subside with decreasing incident energy, from the $E_i = B_K$ ($\chi_1 = 1$) resonance value towards lower energies (Table II).

For the ID region (low-energy part of the spectra), a good qualitative agreement with the theory is also observed: namely the narrowing ID half-width which increases with the incident energy in an almost symmetric way to the high-energy front. For this region, the experimental absolute differential cross sections seem consistently larger (5–10 times) than the theoretical predictions on all the spectra, like in the case of K-shell RRCS,[17,18] a fact still unexplained for the moment. This may be partly due to the approximations used in the calculations such as nonrelativistic dipolar approximation and the hydrogenic atom.

Due to the continuous nature of the synchrotron radiation, a higher-order harmonic appears in the spectrum from the monochromator. The second harmonic ($2E$) radiation is of interest here, as it may induce ID on the K-shell electrons. By measuring the $E/2E$ ratio in our experiment we estimate this contribution to be negligible.

A cause of the disagreement between theory and experiment at low energy could be the M-shell (and N-shell) infrared divergence. The Raman-Compton scattering contribution of the M shell has been observed on the high-energy end of the spectrum by Kodre and Shafroth[19] on solid targets and estimated to be approximately 20% of the L-shell contribution. Unfortunately, being so close to the Rayleigh and Compton peaks these features could not be observed in our spectra. However, as the ID end of the spectrum mimics the behavior of the RRCS end, it is expected that the contributions to the ID of the M and N shell are not negligible but nevertheless weak. Indeed, using formulas 45 and 46 from Åberg and Tulkki[6] we were able to estimate the theoretical relative contributions of the L and M shells to the ID spectrum (see Fig. 10). With the inelastic scattering cross section of the L and M shells scaling like the photoionization cross sections, and using a code by Cromer and Liberman,[20] we estimated the M-shell contribution to the ID to be less than 15% of the L-shell contribution, which cannot account for the large discrepancy we found between theory and experiment.

TABLE II. Comparison between experimental and theoretical RRC differential cross sections as a function of the incident photon energy in threshold units.

$\chi_1 = E_1/B_K$	$\frac{\mathcal{N}_{\text{expt}} - \mathcal{N}_{\text{Theor}}}{\mathcal{N}_{\text{Th}}}$ (%)
0.96	27
0.88	30
0.82	48
0.77	55

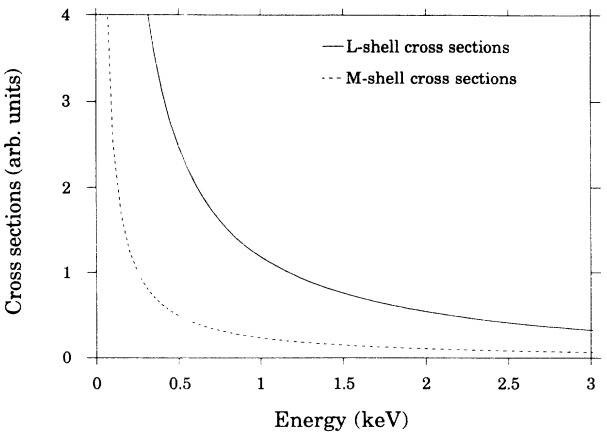

FIG. 10. L- and M-shell ID differential cross sections as a function of the scattered photon energy (from Ref. 6).

The only comparable result found in the literature for L electrons is that of Bannett *et al.*,[12] who measured the total cross section of the RRCS using the Cu $K\alpha$ radiation from an x-ray tube on various Z targets (Ge, Ga, Zn, Cu, Ni). Their target thicknesses being very large compared to the range of the L photoelectrons, they recorded a very strong bremsstrahlung which they tried to correct for by using a thick target formula of the literature (Ref. 21). Their result is, however, very sensitive to an experimental parameter k which models the bremsstrahlung and they only observed the RRC shape and a plateau at intermediate energies, coming from constructive interferences between the ID and RRC processes. Moreover, the energy cutoff (1.5 keV) of their detecting setup prevented them from observing the energy region where the ID was expected for these targets (1.5–2.5 keV). Their overall results exhibit a disagreement with Gavrila and Tugulea's calculations by a factor of 2 on a large range of energies: $0.7 < \chi < 0.9$ in threshold energies ($\chi = E/B_K$). In one case (Ni, $\chi \approx 0.95$) the theory-experiment discrepancy is only 25%, in very good agreement with our results (27% for $\chi \approx 0.96$). In this case direct comparison with Gavrila and Tugulea's unpolarized results is unwarranted as their x-ray beam is partially polarized after the LiF monochromator they used. Furthermore, as explained earlier (see Sec. II B) the nonresonant A^2 term in the scattering cannot be neglected in this case.

A similar series of experiments has been performed by Kane and Baba Prasad[17] and Basavaraju *et al.*[18] on K electrons using γ radiation from radioactive sources (279.2 keV) and thick Au and Sn targets. The authors have also found an ID larger by about an order of magnitude than that of Gavrila and Tugulea's calculations. This result has been recently criticized by Marchetti and Franck,[22] who claimed that this low-energy tail could be due to bremsstrahlung in very thick targets.

Finally, experimental results obtained by Spitale and Bloom[23] in a coincidence setup using γ-ray techniques and thick targets (Fe, Sn, Au, Ho) also recorded the same factor of 10 difference from Gavrila and Tugulea's results for the ID region. While reasonable agreement on the high-energy shape of the RRC scattering spectrum seems

to have been found (this work), this huge discrepancy on the ID still remains unexplained.

ACKNOWLEDGMENTS

The authors would like to express their gratitude to Dr. M. Gavrila and Professor T. Åberg for the numerous helpful discussions and advice for this work, to the staff of DCI for good running conditions, and to Y. Petroff for his support and kind encouragement. The Laboratoire de Physique Atomique et Nucléaire–Institut du Radium is "unité associée No. 771 au Centre National de la Recherche Scientifique."

---

*Present address: Lawrence Livermore National Laboratory, L-417, P.O. Box 808, Livermore, CA 94550.

†Present address: National Institute of Standards and Technology, Gaithersburg, MD 20899.

[1]K. Das Gupta, Phys. Rev. Lett. **3**, 38 (1959).

[2]C. J. Sparks Jr., Phys. Rev. Lett. **33**, 262 (1974).

[3]J. P. Briand, D. Girard, V. Kostroun, P. Chevallier, K. Wohrer, and J. P. Mossé, Phys. Rev. Lett. **46**, 1625 (1981).

[4]J. P. Briand, A. Simionovici, P. Chevallier, and P. Indelicato, Phys. Rev. Lett. **62**, 2092 (1989).

[5]J. J. Sakurai, *Advanced Quantum Mechanics* (Addison-Wesley, Reading, MA, 1967), Chap. II.

[6]T. Åberg and J. Tulkki, in *Atomic Inner Shell Physics,* edited by B. Crasemann (Plenum, New York, 1985).

[7]P. Eisenberger, P. M. Platzmann, and H. Winick, Phys. Rev. B **13**, 2377 (1976).

[8]P. Suortti, Phys. Status Solidi B **91**, 657 (1979).

[9]J. Tulkki and T. Åberg, J. Phys. B **15**, L435 (1982).

[10]Reference to these unpublished results is made by R. D. Deslattes in J. Phys. (Paris) Colloq. **48**, C9-579 (1987).

[11]M. Gavrila and M. N. Tugulea, Rev. Roum. Phys. **20**, 209 (1975).

[12]Y. Bannett, D. C. Rappaport, and I. Freund, Phys. Rev. A **16**, 2011 (1977).

[13]A. Simionovici, Ph.D. dissertation, University of Paris XI, Orsay France, 1988.

[14]Wm. J. Veigele, At. Data Nucl. Data Tables **5**, 51 (1973).

[15]L. Katz and A. S. Penfold, Rev. Mod. Phys. **31**, 920 (1952).

[16]T. Tabata, R. Ito, and S. Okabe, Nucl. Instrum. Methods **103**, 85 (1972).

[17]P. P. Kane and P. N. Baba Prasad, Phys. Rev A **15**, 1976 (1977).

[18]G. Basavaraju, P. P. Kane, and S. M. George, Phys. Rev. A **36**, 655 (1987).

[19]A. F. Kodre and S. M. Shafroth, Phys. Rev. A **19**, 675 (1979).

[20]D. T. Cromer and D. Liberman, Acta Crystallogr. Sect. A **37**, 267 (1981).

[21]R. D. Evans, *The Atomic Nucleus* (McGraw-Hill, New York, 1955), Sec. 21.2.

[22]V. Marchetti, and C. Franck, Phys. Rev. A **39**, 647 (1989).

[23]G. C. Spitale and S. D. Bloom, Phys. Rev. A **16**, 221 (1987).

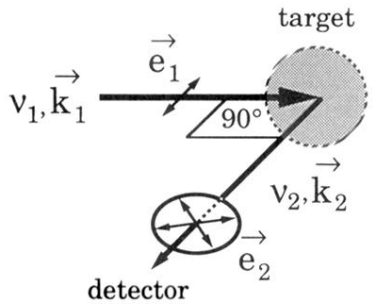

FIG. 3. Schematic of the polarizations and wave vectors for the RRC scattering (see text).

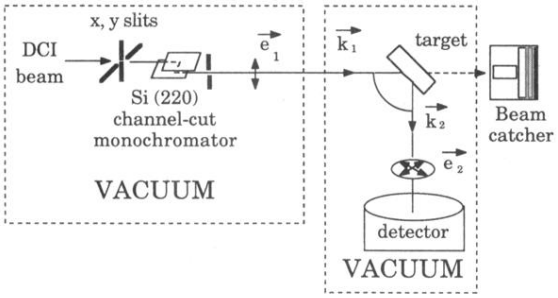

FIG. 5. Schematic of the experimental setup.

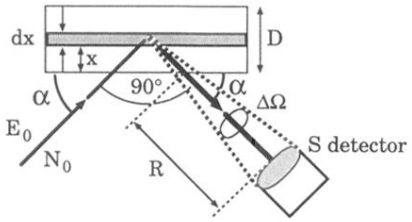

FIG. 8. Schematic of the scattering geometry.